





Position and electric field dependent local lattice strain detected by nanobeam x-ray diffraction on a relaxor ferroelectric single crystal

Shinobu Aoyagi ^{1,*} Ayumi Aoyagi,¹ Hiroaki Takeda ² Hitoshi Osawa,³ Kazushi Sumitani,³ Yasuhiko Imai ³ and Shigeru Kimura ³

¹Department of Information and Basic Science, Nagoya City University, Nagoya 467-8501, Japan

²Department of Applied Chemistry, Faculty of Engineering, Saitama University, 255 Shimoohkubo, Sakura-ku, Saitama 338-8570, Japan

³Center for Synchrotron Radiation Research, Japan Synchrotron Radiation Research Institute, Sayo, Hyogo 679-5198, Japan



(Received 18 September 2021; revised 3 December 2021; accepted 20 December 2021; published 3 January 2022)

Under a static electric field, we present the scanning nanobeam x-ray diffraction of a relaxor ferroelectric single crystal. The x-ray intensity distributions of a Bragg peak in reciprocal space diffracted from local volumes on the surface of a $0.7\text{Pb}(\text{Mg}_{1/3}\text{Nb}_{2/3})\text{O}_3 - 0.3\text{PbTiO}_3$ (PMN-30PT) single crystal show position and electric field dependence. While the spatially averaged intensity distribution has a single peak corresponding to the average crystal structure, intensity distributions from each local volume have several strong sharp peaks and a weak broad peak, and show strong position dependence as the translation symmetry is broken in nano- to microscale. A static local lattice strain with spatially valuable lattice constants and nanodomains is responsible for peak splitting and heterogeneous crystal structure. The locally strained lattice exhibits a significant tensile lattice strain caused by an electric field, which is compatible with its large piezoelectric constant of approximately 2×10^3 pC/N. When the electric field surpasses the coercive field of 3 kV/cm, polarization switching causes a substantial shear lattice strain with intensity redistribution. Position dependence can also be seen in the piezoelectric constants and coercive fields calculated from x-ray diffraction data for each local location. The standard deviation of the local lattice strain distribution is 3×10^{-3} regardless of the electric field, which is greater than the piezoelectric lattice strain of 1×10^{-3} caused by an electric field of 8 kV/cm. The enormous electric field induced lattice strain and fatigue-free polarization switching are enabled and facilitated by the nano- to microscale heterogeneous crystal structure with widely and continuously distributed local lattice strain.

DOI: [10.1103/PhysRevB.105.024101](https://doi.org/10.1103/PhysRevB.105.024101)

I. INTRODUCTION

Lead-based relaxor ferroelectric perovskites, such as $(1-x)\text{Pb}(\text{Mg}_{1/3}\text{Nb}_{2/3})\text{O}_3 - x\text{PbTiO}_3$ (PMN-PT) and $(1-x)\text{Pb}(\text{Zn}_{1/3}\text{Nb}_{2/3})\text{O}_3 - x\text{PbTiO}_3$ (PZN-PT), are widely used in sensors, actuators, and transducers because of their excellent piezoelectric properties [1–3]. Their piezoelectric constants and electromechanical coupling factors are enhanced by a solid solution with tetragonal PbTiO_3 (PT) and have a maximum value near the morphotropic phase boundary (MPB) that separates low-PT rhombohedral and high-PT tetragonal phases [4–8]. The piezoelectric constants of PMN-PT with $x = 0.30$ (PMN-30PT) and PZN-PT with $x = 0.08$ (PZN-8PT) near their MPBs exceed 2×10^3 pC/N [7,8]. Electric field induced phase transitions involving polarization rotation and electric field responses of polar nanoregions (PNRs) aiding the polarization rotation have been proposed as explanations for the enormous piezoelectric capabilities around the MPB [9–24]. Monoclinic and orthorhombic phases exist in a narrow composition region near the MPB and are easily induced by applying an electric field [8,10,11,14,17,18]. PNRs first occur below the Burns temperature in the high-temperature paraelectric

cubic phase, expanding with cooling, and coexisting with regular ferroelectric domains in low-temperature ferroelectric phases [21].

We have recently reported that disordered Pb atoms partially occupying off-center sites show an intersite rotational displacement involving polarization rotation in a PZN-4.5PT single crystal under an electric field [25]. The average crystal structure of the single-crystal size below 0.1 mm was successfully analyzed using a rhombohedral and a monoclinic structure model with disordered Pb atoms under zero and nonzero fields. However, the crystal with PNRs must have a heterogeneous structure in which the lattice is locally strained and the Pb displacements are locally modulated. Actually, heterogeneous spatial distributions of Pb displacements in relaxor ferroelectric perovskites have been found by diffuse and total scattering using x-ray and neutron and transmission electron microscopy [26–29]. Electric field dependence of the heterogeneous local Pb displacements and the local lattice strain is key to understanding the giant piezoelectric properties of relaxor ferroelectric perovskites.

In this study, we used scanning nanobeam x-ray diffraction (XRD) of a single crystal of PMN-30PT under a static electric field to show the position and electric field dependence of the local lattice strain in relaxor ferroelectric perovskites. With high accuracy, scanning nanobeam XRD can visualize a distribution of local lattice strains on a crystal surface [30,31]. The

*aoyagi@nsc.nagoya-cu.ac.jp

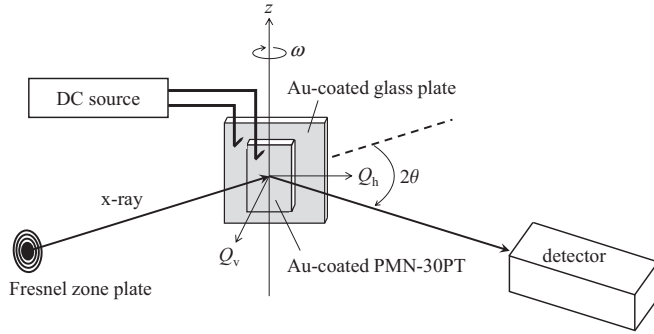


FIG. 1. Experimental layout of the scanning nanobeam XRD of PMN-30PT under a static electric field. The position and electric field dependence of the 002 Bragg intensity distribution from each local volume were measured.

x-ray beam size of 300 nm is much larger than the PNR's size of 20 nm [21]. However, a fractal character has been found in relaxor ferroelectric perovskites by quasielastic light scattering and x-ray diffuse scattering measurements [32,33]. The nanobeam XRD detects submicron scale structural inhomogeneity originating from the fractal character. The scanning nanobeam XRD for PMN-30PT under an electric field in this study provides essential information about the local lattice strain with such a fractal character and its role in giant piezoelectric properties.

II. EXPERIMENT

The scanning nanobeam XRD of a single crystal of PMN-30PT under a static electric field was performed at beamline BL13XU of the SPring-8 large synchrotron radiation facility [34]. A schematic layout of the experiment is shown in Fig. 1. A commercially available [001] oriented thin single-crystal plate of PMN-30PT with surfaces of $3 \times 2 \text{ mm}^2$ coated by Au electrodes and a thickness of 0.1 mm was used in the experiment. The Au-coated PMN-30PT single crystal attached on an Au-coated glass plate using silver paste was mounted on a nanobeam x-ray diffractometer to be the crystal surface perpendicular to the horizontal plane and parallel to the incident x-ray beam axis at the crystal orientation angle $\omega = 0$. Static electric fields from $E = -8$ to 8 kV/cm were applied along [001] perpendicular to the crystal surface using a DC source and micropositioning probes.

The incident x-ray beam with a wavelength of $\lambda = 1.55 \text{ \AA}$ was focused on the crystal surface using a Fresnel zone plate. The penetration depth of the x ray is $7 \mu\text{m}$ for PMN-30PT. The x-ray beam size at the sample position was 430 (horizontal) \times 190 (vertical) nm^2 at the full width at half maximum (FWHM). A motorized sample stage can scan the beam position on the crystal surface. Only the vertical position z was scanned from 0 to $10 \mu\text{m}$ in this study. X-ray intensities diffracted by the (002) lattice plane of the PMN-30PT single crystal were measured in reflection geometry using a Timepix STPX -65k (Amsterdam Scientific Instruments BV) two-dimensional hybrid pixel detector located at a diffraction angle of $2\theta = 45.2^\circ$ and a camera length of $L = 338 \text{ mm}$. The crystal orientation angle ω was scanned in steps of 0.005° . Integrating x-ray intensities on the detector along the vertical

direction yielded two-dimensional reciprocal space maps of x-ray intensities on the horizontal plane for each z position.

We also performed nanobeam XRD experiments for another [001] oriented thin single-crystal plate of PMN-30PT before and after coating with Au electrodes to evaluate surface topography effects. The nanobeam x-ray with shorter wavelength of $\lambda = 0.95 \text{ \AA}$ and larger penetration depth of $11 \mu\text{m}$ was used to reduce contributions of the surface region to the x-ray diffraction intensities. X-ray intensities diffracted by the (004) lattice plane were measured using an x-ray VHR 1.00:1 (Photonic Science Ltd.) charge-coupled device detector located at $2\theta = 56.0^\circ$ and $L = 279 \text{ mm}$. The crystal orientation angle ω was scanned in steps of 0.01° .

Single-crystal XRD also determined the average crystal structure of PMN-30PT at beamline BL02B1 of SPring-8 [35]. A single crystal of PMN-30PT with $0.07 \times 0.06 \times 0.04 \text{ mm}^3$ was used in the experiment. A high-energy x ray with a wavelength of $\lambda = 0.30 \text{ \AA}$ was used to reduce the absorption effects of Pb atoms and extinction effects. The penetration depth of 0.12 mm and the beam size of 0.2 mm are larger than the crystal size. The single-crystal XRD patterns were collected in transmission geometry by using a large cylindrical imaging plate camera with a radius of 191.3 mm. Intensities of the Bragg peak unsplit and split by ferroelectric domain twinning were integrated to obtain sums of integrated intensities of multiple domains. For example, x-ray intensity distributions of unsplit and split Bragg peaks recorded on the imaging plate are shown in Figs. 2(a) and 2(b), respectively. The unsplit 00 l and split hhh Bragg peaks can be explained by a multiple twinning of eight pseudocubic rhombohedral domains with the polar threefold axis along $[111]$, $[\bar{1}\bar{1}\bar{1}]$, $[\bar{1}\bar{1}1]$, $[\bar{1}1\bar{1}]$, $[11\bar{1}]$, $[1\bar{1}1]$, $[111]$, and $[\bar{1}\bar{1}\bar{1}]$.

III. RESULTS AND DISCUSSION

A. Average crystal structure analysis

The average crystal structure of the PMN-30PT single crystal was analyzed using a Pb-disordered rhombohedral structure model with eight ferroelectric domains similar to the previously reported average crystal structure analysis of PZN-4.5PT [25]. Pb atoms partially occupy four fractional positions in the structure model, $(\Delta x_{\text{Pb}}, \Delta x_{\text{Pb}}, \Delta x_{\text{Pb}})$, $(\Delta x_{\text{Pb}}, \Delta x_{\text{Pb}}, -\Delta x_{\text{Pb}})$, $(\Delta x_{\text{Pb}}, -\Delta x_{\text{Pb}}, \Delta x_{\text{Pb}})$, and $(-\Delta x_{\text{Pb}}, \Delta x_{\text{Pb}}, \Delta x_{\text{Pb}})$. The first position Pb(1) is on the polar threefold axis along $[111]$, and the latter three positions Pb(2) are equivalent in the rhombohedral structure with space group $R3m$. The site occupancies at Pb(1) (g_{Pb1}) and Pb(2) (g_{Pb2}) are not identical and have a relation of $g_{\text{Pb1}} = 1 - 3g_{\text{Pb2}}$. Without positional disorder, the chemically disordered Mg, Nb, and Ti (B) atoms occupy the body-centered position (0.5, 0.5, 0.5). O atoms occupy three equivalent positions near the face-centered positions $(0.5 + \Delta x_{\text{O}}, 0.5 + \Delta x_{\text{O}}, \Delta z_{\text{O}})$, $(0.5 + \Delta x_{\text{O}}, \Delta z_{\text{O}}, 0.5 + \Delta x_{\text{O}})$, and $(\Delta z_{\text{O}}, 0.5 + \Delta x_{\text{O}}, 0.5 + \Delta x_{\text{O}})$ without positional disorder. Volume ratios of eight domains, site occupancies of the disordered Pb atom (g_{Pb1} and g_{Pb2}), atomic displacements of the Pb and O atoms (Δx_{Pb} , Δx_{O} , and Δz_{O}), and anisotropic atomic displacement parameters (U_{ij}) of all atoms were refined by full-matrix least-squares analysis using SHELXL [36]. The result of the average structure analysis of PMN-30PT is

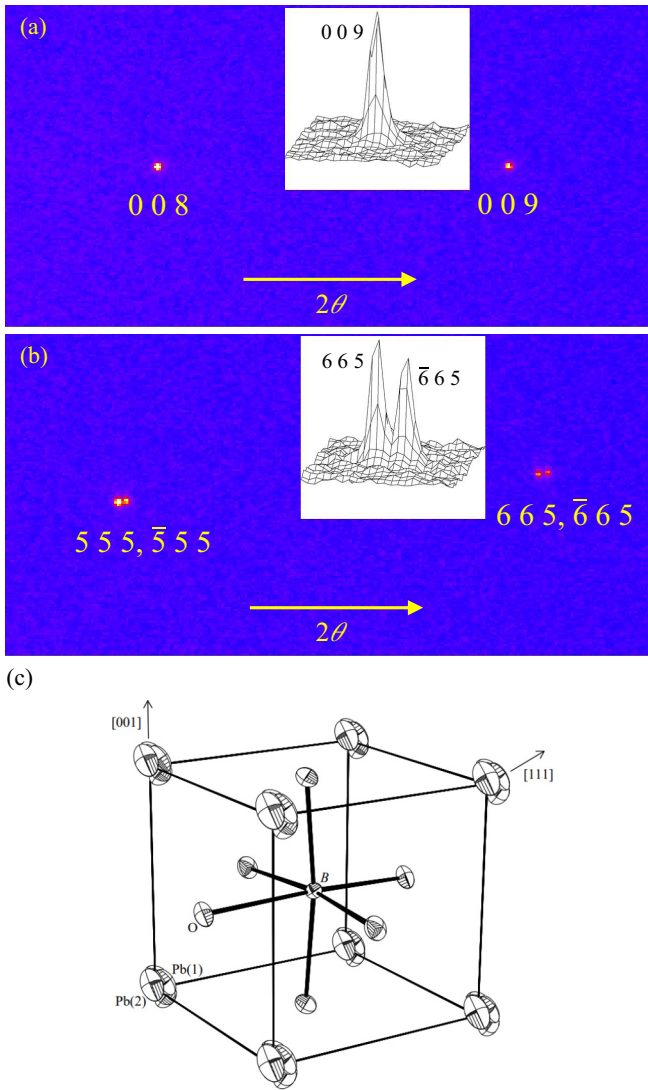


FIG. 2. X-ray intensity distributions of (a) unsplit and (b) split Bragg peaks of a whole crystal of PMN-30PT measured using unfocused x rays and a cylindrical imaging plate. Vertical and horizontal axes are parallel to the cylindrical and 2θ axes, respectively. One pixel size is 0.03° in 2θ which corresponds to about 0.01 \AA^{-1} in $Q = 4\pi \sin(\theta)/\lambda$. (c) The average rhombohedral crystal structure model of PMN-30PT with atomic displacement ellipsoids at 50% probability level. The atom labeled B is chemically disordered Mg, Nb, and Ti.

summarized in Table I with that of PZN-4.5PT for a comparison. The experimental and analytical conditions of the two crystals are almost the same. Figure 2(c) shows the refined average rhombohedral crystal structure model of PMN-30PT with disordered Pb atoms.

The average rhombohedral structure of PMN-30PT is similar to that of PZN-4.5PT as shown in Table I. It is noticed that g_{Pb1} is larger than g_{Pb2} in PMN-30PT, and vice versa in PZN-4.5PT. The bond lengths of shorter Pb-O bonds in both materials ($\sim 2.53 \text{ \AA}$) are comparable to that of a covalent Pb-O bond in the tetragonal PbTiO_3 (2.51 \AA) [37]; hence they have a covalent character. The structural similarity suggests that disordered Pb atoms in PMN-30PT also show an intersite ro-

tational displacement involving polarization rotation under an electric field as observed in PZN-4.5PT [25]. Time-resolved average crystal structure analyses of PMN-30PT under an alternating electric field are also progressing and will be reported soon.

B. Local lattice strain distribution

Although PMN-30PT has a rhombohedral crystal structure on a time and space average, the scanning nanobeam XRD experiment shows a heterogeneous lattice strain distribution. Figures 3(a) and 3(b) show the intensity distribution of the 002 Bragg peak of PMN-30PT in the $Q_h Q_v$ reciprocal space as a function of position (z) dependence under static electric fields of $E = -8$ and 0 kV/cm , respectively. Q_h and Q_v are reciprocal axes in the horizontal plane parallel and perpendicular to the crystal surface, respectively (Fig. 1). The numerical values are given by the formulas $Q_h = Q \sin(\omega - \theta)$ and $Q_v = Q \cos(\omega - \theta)$ where $Q = 4\pi \sin(\theta)/\lambda$ is the scattering vector length in units of \AA^{-1} . We measured the data from $z = 0$ to $10 \mu\text{m}$ with a step of $0.5 \mu\text{m}$ at -8 kV/cm first, -4 kV/cm second, and 0 kV/cm finally. Regardless of the electric field, unusual position dependence of the intensity distribution breaking the translation symmetry was detected, as shown in the figures.

Figures 4(a) and 4(b) show the position dependence of Q_h and Q_v one-dimensional 002 Bragg profiles of PMN-30PT at $E = 0 \text{ kV/cm}$ through the intensity maximum points, respectively. Unlike the average 009 Bragg profile shown in Fig. 2(a), the local 002 Bragg profiles have several strong sharp peaks and a weak broad peak, and show strong position dependence. Therefore, nanodomains with various lattice constants and orientations exist in the measured local volume, and the translation symmetry breaks in microscale. A few nanodomains with larger volumes in the local volume contribute to strong, sharp peaks. However, smaller nanodomains with various lattice constants and orientations contribute to a weak broad peak. The average intensity distributions obtained by averaging the 21 intensity distributions through $z = 0 - 10 \mu\text{m}$ are also shown at the bottom of Figs. 3 and 4. They have a nearly single peak shape consistent with the $00l$ Bragg peak shape of the whole crystal with the volume of $0.07 \times 0.06 \times 0.04 \text{ mm}^3$ shown in Fig. 2(a), suggesting that the average crystal structure is rhombohedral in $10 \mu\text{m}$ scale.

As shown in Fig. 3, the intensity distributions do not change significantly when the electric field is reduced from -8 to 0 kV/cm . Therefore, the spatial distribution of nanodomains is static and slightly responds to an electric field along $[001]$. This fact is consistent with the previously reported neutron diffuse scattering measurement result under a $[001]$ field [38]. It has been reported in the paper that a $[001]$ field only affects some PNRs, and the magnitude of redistribution of PNRs is smaller for a $[001]$ field than that for a $[111]$ field parallel to the polarization axis.

Mean values of shear lattice strain $s_h(z, E)$ and tensile lattice strain $s_v(z, E)$ of the (002) lattice plane within each local volume at position z and electric field E were estimated

TABLE I. Summary of the average rhombohedral structure analyses of PMN-30PT and PZN-4.5PT under zero field at room temperature. a and α are rhombohedral lattice constants. N is the number of independent Bragg intensities used in the analysis. n is the number of refined parameters. R , R_w , and S are the reliable factor based on absolute structure factors, the weighted reliable factor based on squared structure factors, and the least-squares goodness of fit parameter, respectively. B means chemically disordered Mg (Zn), Nb, and Ti atoms.

Crystal	a (Å)	α (deg)	N	n	R	R_w	S
PMN-30PT	4.028(1)	89.92(1)	834	21	0.0329	0.0737	1.081
PZN-4.5PT	4.064(1)	89.94(1)	851	21	0.0246	0.0593	1.068
Crystal	Δx_{Pb}	g_{Pb1}		g_{Pb2}		Δx_{O}	Δz_{O}
PMN-30PT	0.033(1)	0.40(2)		0.198(7)		-0.02315(2)	-0.01304(2)
PZN-4.5PT	0.039(1)	0.231(14)		0.256(5)		-0.02208(2)	-0.01537(2)
Crystal					U_{ij} (Å ²)		
	Pb(1)		Pb(2)		B	O	
PMN-30PT	$U_{11} = 0.0193(8)$ $U_{23} = -0.0069(3)$		$U_{11} = 0.0263(6)$ $U_{33} = 0.0142(6)$ $U_{23} = 0.0014(3)$ $U_{12} = -0.0133(6)$		$U_{11} = 0.00809(15)$ $U_{23} = 0.00046(19)$	$U_{11} = 0.0165(8)$ $U_{33} = 0.0105(7)$ $U_{23} = -0.0018(6)$ $U_{12} = -0.0027(8)$	
PZN-4.5PT	$U_{11} = 0.0207(11)$ $U_{23} = 0.0031(9)$		$U_{11} = 0.0313(7)$ $U_{33} = 0.0222(6)$ $U_{23} = 0.0038(4)$ $U_{12} = -0.0199(7)$		$U_{11} = 0.01152(13)$ $U_{23} = 0.0008(6)$	$U_{11} = 0.0294(11)$ $U_{33} = 0.0155(11)$ $U_{23} = -0.0008(12)$ $U_{12} = -0.008(3)$	
Crystal	Pb(1)-O (Å)		Pb(2)-O (Å)		B -O (Å)		
PMN-30PT	2.5366(7)		2.5316(7) 2.6681(7)		1.9657(5) 2.0710(5)		
PZN-4.5PT	2.5333(6)		2.5259(7) 2.6604(7)		1.9734(5) 2.0985(5)		

using the following equations.

$$s_h(z, E) = \frac{\langle Q_h \rangle(z, E)}{\langle Q_v \rangle(0, 0)}, \quad s_v(z, E) = 1 - \frac{\langle Q_v \rangle(z, E)}{\langle Q_v \rangle(0, 0)}, \quad (1)$$

$$\langle Q_h \rangle(z, E) = \frac{\sum_{\omega, 2\theta} Q_h(z, E, \omega, 2\theta) I(z, E, \omega, 2\theta)}{\sum_{\omega, 2\theta} I(z, E, \omega, 2\theta)}, \quad \langle Q_v \rangle(z, E) = \frac{\sum_{\omega, 2\theta} Q_v(z, E, \omega, 2\theta) I(z, E, \omega, 2\theta)}{\sum_{\omega, 2\theta} I(z, E, \omega, 2\theta)}, \quad (2)$$

$$\sigma_h(z, E) = \frac{1}{\langle Q_v \rangle(z, E)} \sqrt{\frac{\sum_{\omega, 2\theta} [Q_h(z, E, \omega, 2\theta) - \langle Q_h \rangle(z, E)]^2 I(z, E, \omega, 2\theta)}{\sum_{\omega, 2\theta} I(z, E, \omega, 2\theta)}},$$

$$\sigma_v(z, E) = \frac{1}{\langle Q_v \rangle(z, E)} \sqrt{\frac{\sum_{\omega, 2\theta} [Q_v(z, E, \omega, 2\theta) - \langle Q_v \rangle(z, E)]^2 I(z, E, \omega, 2\theta)}{\sum_{\omega, 2\theta} I(z, E, \omega, 2\theta)}}. \quad (3)$$

$Q_h(z, E, \omega, 2\theta)$ and $Q_v(z, E, \omega, 2\theta)$ are reciprocal coordinates, and $I(z, E, \omega, 2\theta)$ is a background-subtracted intensity at diffractometer angles ω and 2θ in the two-dimensional reciprocal space intensity maps measured at position z and electric field E . $\sigma_h(z, E)$ and $\sigma_v(z, E)$ are normalized standard deviations of each intensity distribution along Q_h and Q_v , respectively, which are normalized by $\langle Q_v \rangle(z, E)$.

The local lattice strains $s_h(z, E)$ and $s_v(z, E)$ show strong position (z) dependence regardless of the electric field E , as shown in Fig. 5. Differences between the maximum and minimum local lattice strains through $z = 0 - 10 \mu\text{m}$ at a

fixed electric field are 0.9×10^{-3} for $s_h(z, E)$ and 1.8×10^{-3} for $s_v(z, E)$. These values are comparable to $\sigma_h(z, E)$ and $\sigma_v(z, E)$, which show almost no position and electric field dependence and have values of 2×10^{-3} and 3×10^{-3} , respectively. $s_h(z, E)$ and $s_v(z, E)$ are constant and decreased, respectively, with removing an electric field from -8 to 0 kV/cm regardless of the position z . The tensile strain $s_v(z, E)$ under an electric field along $[001]$ causes a monoclinic deformation of the rhombohedral lattice breaking the threefold symmetry. The average difference between $s_v(z, -8)$ and $s_v(z, 0)$ is 0.8×10^{-3} which is smaller than $\sigma_v(z, E)$ of 3×10^{-3} . Therefore, the standard deviations of

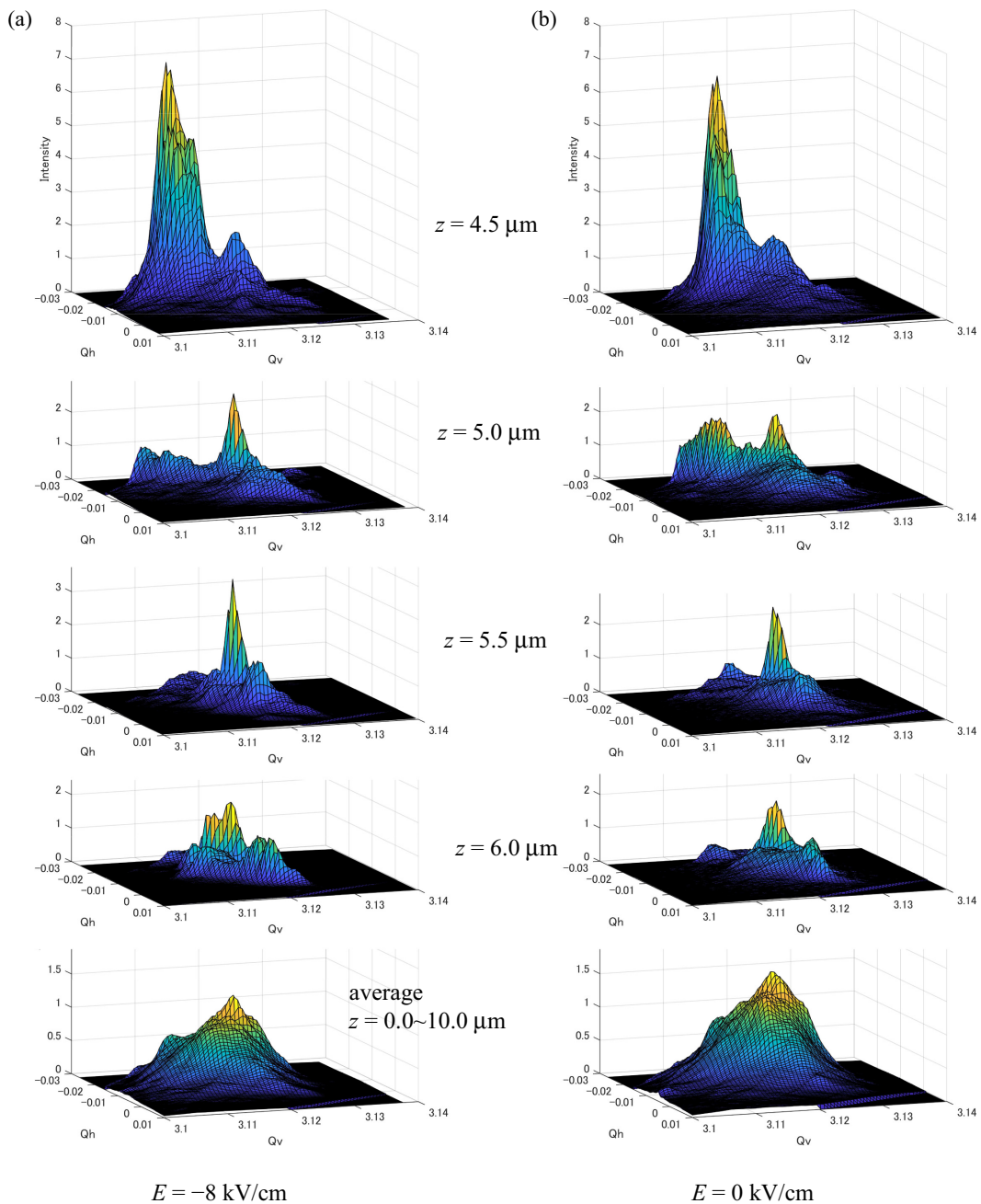


FIG. 3. Position (z) dependence of x-ray intensity distributions of 002 Bragg peak of PMN-30PT in the $Q_h Q_v$ reciprocal space under static electric fields of (a) $E = -8$ and (b) 0 kV/cm. The average intensity distributions obtained by averaging the 21 intensity distributions through $z = 0 - 10 \mu\text{m}$ are also shown at the bottom.

the local lattice strain distribution under zero field are surprisingly larger than the piezoelectric lattice strain induced by an 8 kV/cm electric field.

Q_h and Q_v one-dimensional 004 Bragg profiles measured for another PMN-30PT single crystal before and after coating with Au electrodes using the shorter wavelength x ray with $\lambda = 0.95 \text{ \AA}$ also show similar position dependences as shown in Fig. 6. The results support that the position dependent local lattice strain exists not only in the surface region but also in the bulk region regardless of the Au surface electrodes. The deeper bulk region below the surface contributes to the diffracted intensities in the experimental condition using the

x ray with larger penetration depth although the contribution of the surface region is not completely eliminated. The difference in the local lattice strain distribution between the surface and bulk regions, surface treatment effects, and also sample dependences should be studied in detail.

C. Field-induced local lattice strain

In addition to the piezoelectric lattice strain, polarization switching resulted in an intensity redistribution and a peak shift. Figures 7(a) and 7(b) show the intensity distribution of the 002 Bragg peak of PMN-30PT in the $Q_h Q_v$ reciprocal

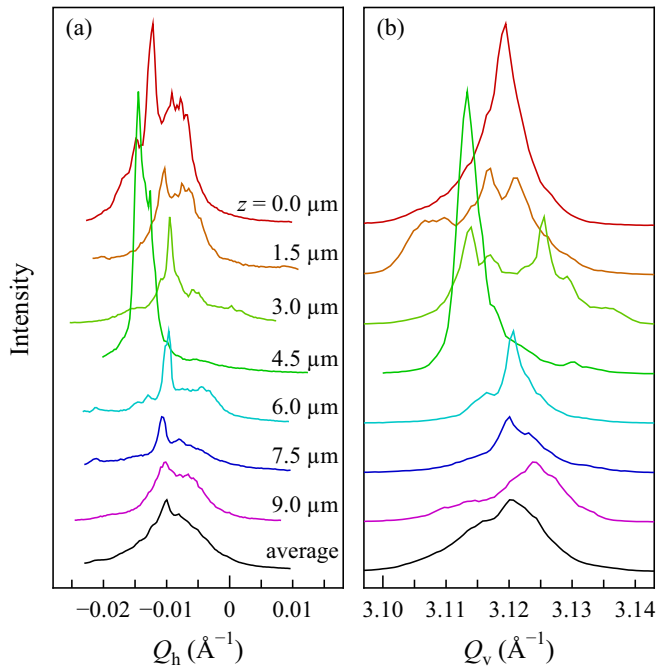


FIG. 4. Position (z) dependence of (a) Q_h and (b) Q_v one-dimensional 002 Bragg profiles of PMN-30PT at $E = 0$ kV/cm through the intensity maximum points. The average intensity profiles obtained by averaging the 21 intensity distributions through $z = 0 - 10$ μm are also shown at the bottom.

space at position $z = 0$ and 2.5 μm , respectively, as a function of electric field (E). We measured the data by changing E from -8 to 8 kV/cm and then backing to -8 kV/cm at each position $z = 0, 2.5, 5.0, 7.5,$ and 10 μm . As shown in the

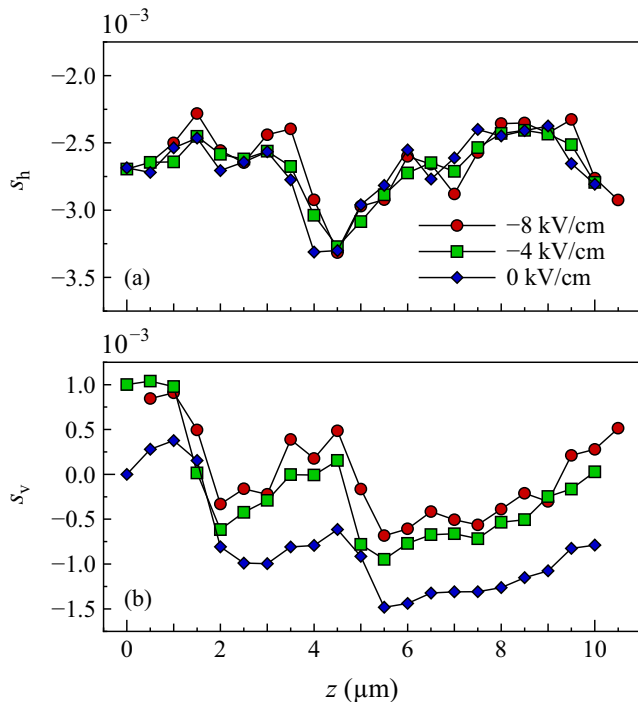


FIG. 5. Position (z) dependence of (a) shear local lattice strain $s_h(z, E)$ and (b) tensile local lattice strain $s_v(z, E)$ of the (002) lattice plane of PMN-30PT at $E = -8, -4,$ and 0 kV/cm.

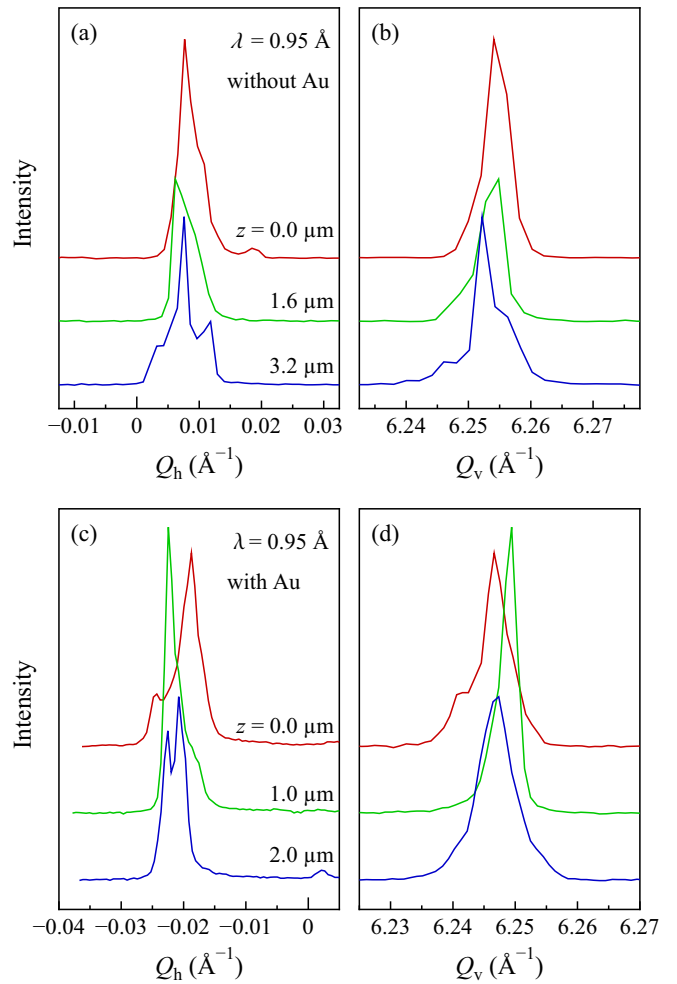


FIG. 6. Position (z) dependence of (a), (c) Q_h and (b), (d) Q_v one-dimensional 004 Bragg profiles through the intensity maximum points measured for another PMN-30PT before (a), (b) and after (c), (d) coating with Au electrodes using the shorter wavelength x ray to reduce surface effects.

figures, the intensity distributions at 0 kV/cm observed in the forward process are obviously different from those observed in the backward process.

Figures 8(a) and 8(b) show the electric field dependence of Q_h and Q_v one-dimensional 002 Bragg profiles of PMN-30PT at $z = 0$ μm through the intensity maximum points, respectively. Discontinuous peak shifts along Q_h with intensity redistributions were observed between $E = 2$ and 4 kV/cm in the forward process and between -2 and -4 kV/cm in the backward process. As shown in Fig. 9, this behavior is explained by polarization switching of a ferroelectric domain with a discontinuous shear deformation of the average rhombohedral lattice and redistribution of polar nanodomains with a heterogeneous structure, which breaks the translation symmetry in the nano- to microscale. The switching of polarization orientation from $[11\bar{1}]$ to $[111]$ accompanies an intersite rotational displacement of disordered Pb atoms and a discontinuous shear lattice deformation with the deformation angle of $0.2^\circ = 2(90 - \alpha)$ [Fig. 9(a)]. The polarization switching process entails a fractal redistribution of

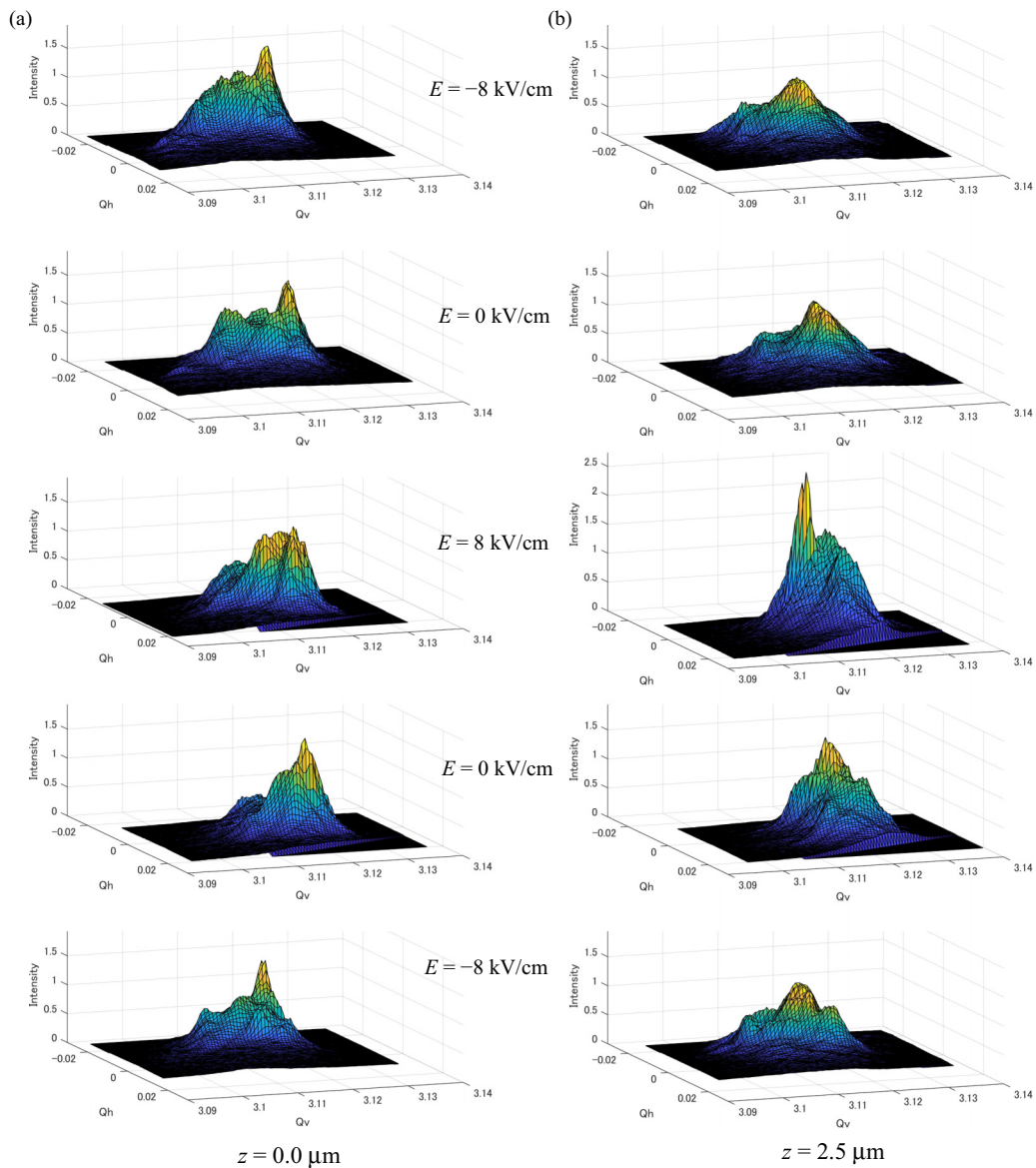


FIG. 7. Electric field (E) dependence of x-ray intensity distributions of 002 Bragg peak of PMN-30PT in the Q_hQ_v reciprocal space at (a) $z = 0$ and (b) $2.5 \mu\text{m}$.

heterogeneous nanodomains spanning throughout the nano- to microscale with varying polarization magnitudes and orientations [Fig. 9(b)].

Figure 10(a) shows the electric field (E) dependence of $s_h(z, E)$ measured at $z = 0, 5,$ and $10 \mu\text{m}$. The shear local lattice strains $s_h(z, E)$ are nearly constant with changing electric field from -8 to 2 kV/cm in the forward process and from 8 to -2 kV/cm in the backward process. The rhombohedral multidomain crystal poled along $[001]$ forms a domain structure consisting of four domains with the polarization along $[111], [\bar{1}\bar{1}\bar{1}], [1\bar{1}\bar{1}],$ and $[\bar{1}\bar{1}1]$, and has an average macroscopic symmetry of $4mm$. In the symmetry, shear piezoelectric strains under an electric field along the fourfold axis parallel to $[001]$ are not allowed. However, when the electric field exceeds the coercive field around $\pm 3 \text{ kV/cm}$, $s_h(z, E)$ is discontinuously changed by about $\pm 3 \times 10^{-3}$. The amount of change in $s_h(z, E)$ is consistent with the rhombohedral

shear lattice strain of $2 \tan(90 - \alpha)$ induced by the polarization switching [Fig. 9(a)] and slightly larger than $\sigma_h(z, E)$ of 2×10^{-3} . Similar switching behavior of $s_h(z, E)$ was observed in common at positions from $z = 0$ to $10 \mu\text{m}$. As a result, in the measured local volume, the crystal appears to be a ferroelectrically single domain. In a ferroelectric domain with an orientation obtained by 180° rotation around $[001]$, the switching behavior of $s_h(z, E)$ will be inverted. In the forward and backward processes, absolute electric fields at $s_h(z, E) = 0$ were averaged to estimate the coercive fields for polarization switching. The obtained coercive fields show some position dependence with values ranging from 2.4 to 2.8 kV/cm .

Figure 10(b) shows the electric field (E) dependence of $s_v(z, E)$ measured at $z = 0, 5,$ and $10 \mu\text{m}$. The local tensile lattice strain $s_v(z, E)$ is linearly decreased with changing electric field from -8 to 2 kV/cm in the forward process and from

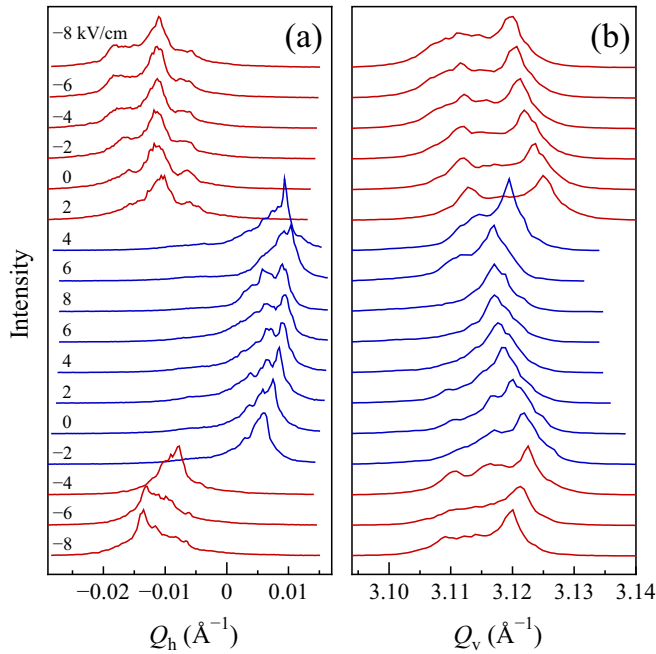


FIG. 8. Electric field (E) dependences of (a) Q_h and (b) Q_v one-dimensional 002 Bragg profiles of PMN-30PT at $z = 0 \mu\text{m}$ through the intensity maximum points.

8 to -2 kV/cm in the backward process. After the electric field reaches the coercive field around $\pm 3 \text{ kV/cm}$, $s_v(z, E)$ is increased by about 1.0×10^{-3} with changing electric field from the coercive fields to $\pm 8 \text{ kV/cm}$. The amount of change in $s_v(z, E)$ is consistent with the piezoelectric strain calculated from the piezoelectric constant of $2 \times 10^3 \text{ pC/N}$, and smaller than $\sigma_v(z, E)$ of 3×10^{-3} . In the forward and backward pro-

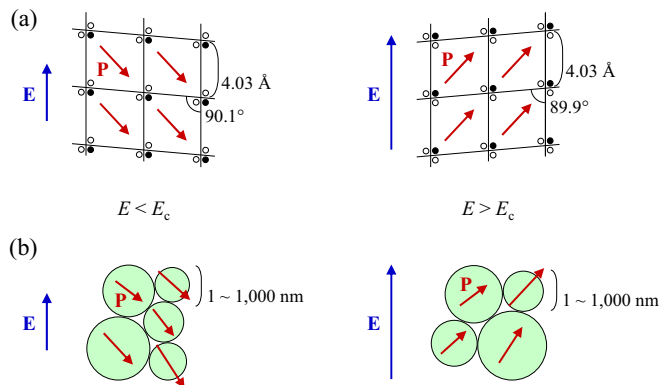


FIG. 9. Schematic drawing of (a) the average structure of the rhombohedral lattice and (b) the heterogeneous structure of the polar nanodomains when the electric field E along $[001]$ is smaller (left) and larger (right) than the coercive field $E_c (>0)$. \mathbf{E} and \mathbf{P} vectors show electric field and polarization, respectively. The rhombohedral lattice viewed along $[100]$ is drawn by solid lines in (a), deformed to a monoclinic lattice under the electric field. Pb(1) and Pb(2) atoms in the rhombohedral structure are drawn by solid and open circles in (a), respectively. Polar nanodomains drawn by circles in (b) have polarizations slightly different in magnitude and orientation with each other.

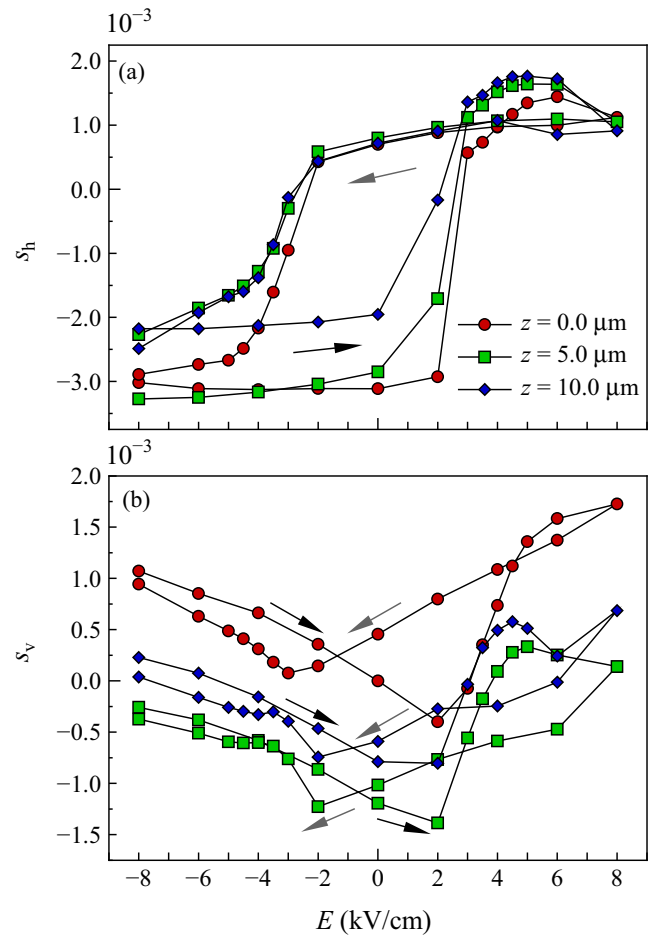


FIG. 10. Electric field (E) dependences of (a) shear local lattice strain $s_h(z, E)$ and (b) tensile local lattice strain $s_v(z, E)$ of the (002) lattice plane of PMN-30PT at $z = 0, 5.0,$ and $10 \mu\text{m}$. The black and gray arrows indicate directions of the forward and backward processes, respectively.

cesses, absolute electric field gradients of $s_v(z, E)$ at $E = 0$ were averaged to estimate the piezoelectric constants. The obtained piezoelectric constants show some position dependence with values ranging from 1.4×10^3 to $1.8 \times 10^3 \text{ pC/N}$.

The fractal character of relaxor ferroelectric perovskites is demonstrated in this study by the heterogeneous lattice strain distribution in the nano- to microscale. Although the intensity distributions averaged through $z = 0 - 10 \mu\text{m}$ exhibit a single peak shape consistent with the average rhombohedral structure (Figs. 3 and 4), a large-scale heterogeneous structure in the crystal might be found in a further nanobeam XRD measurement on a larger volume. The standard deviations of the local lattice strain distribution near the surface are larger than the piezoelectric lattice strain induced by an electric field of 8 kV/cm . The widely and continuously distributed local lattice strain spread in nano- to microscale with a fractal character would facilitate the giant piezoelectric strain and the fatigue-free polarization switching. The position dependence of the coercive field and the piezoelectric constant found in this study demonstrate that the heterogeneous structure affects the ferroelectricity and piezoelectricity.

IV. CONCLUSIONS

We used scanning nanobeam XRD under a static electric field along [001] to disclose the position and electric field dependence of the local lattice strain on the surface of a [001] oriented PMN-30PT single-crystal plate. The intensity distributions from each local volume show strong position dependence with the breaking of the translation symmetry. The heterogeneous lattice strain distribution in nano- to microscale proves the fractal character of relaxor ferroelectric perovskites. The locally strained lattice exhibits a large tensile lattice strain due to the inverse piezoelectric effect and a discontinuous shear lattice strain with redistribution of nanodomains due to the polarization switching under a static electric field. The nano- to microscale heterogeneous crystal structure with widely and continuously distributed local lattice strain will enable large tensile lattice strain and the discontinuous shear lattice strain. In this study, we investigated the one-dimensional position dependence of the local lattice strain. Further nanobeam XRD measurements of various crystals in two- and three-dimensional spaces on a larger volume

will give us more detailed information about a large-scale heterogeneous structure and the difference in nanostructures between the surface and bulk regions. Similar measurements under an electric field along [011] and [111] also give us useful information to understand polar nanodomains' electric field response properties.

ACKNOWLEDGMENTS

This work was supported by a Grant-in-Aid for Scientific Research from the Japan Society for the Promotion of Science (JSPS) (Grants No. JP16K05017, No. JP19H02797, and No. JP20H05879), Tatematsu Foundation, Toyoaki Scholarship Foundation, Daiko Foundation, and the Research Equipment Sharing Center at the Nagoya City University. The synchrotron radiation experiments were performed at SPring-8 with the approval of the Japan Synchrotron Radiation Research Institute (JASRI) (Proposals No. 2017A1036, No. 2017A1465, No. 2017B1476, No. 2018B1529, No. 2018B1534, and No. 2019A1308).

-
- [1] R. A. Cowley, S. N. Gvasaliya, S. G. Lushnikov, B. Roessli, and G. M. Rotaru, *Adv. Phys.* **60**, 229 (2011).
- [2] S. Zhang and F. Li, *J. Appl. Phys.* **111**, 031301 (2012).
- [3] E. Suna and W. Cao, *Prog. Mater. Sci.* **65**, 124 (2014).
- [4] J. Kuwata, K. Uchino, and S. Nomura, *Jpn. J. Appl. Phys.* **21**, 1298 (1982).
- [5] S.-E. Park and T. R. Shrout, *IEEE Trans. Ultrason., Ferroelect., Freq. Control* **44**, 1140 (1997).
- [6] S.-E. Park and T. R. Shrout, *J. Appl. Phys.* **82**, 1804 (1997).
- [7] R. Zhang, B. Jiang, W. Jiang, and W. Cao, *IEEE Trans. Ultrason., Ferroelect., Freq. Control* **49**, 1622 (2002).
- [8] Y. Guo, H. Luo, D. Ling, H. Xu, T. He, and Z. Yin, *J. Phys: Condens. Matter* **15**, L77 (2003).
- [9] H. Fu and R. E. Cohen, *Nature (London)* **403**, 281 (2000).
- [10] B. Noheda, D. E. Cox, G. Shirane, S.-E. Park, L. E. Cross, and Z. Zhong, *Phys. Rev. Lett.* **86**, 3891 (2001).
- [11] R. R. Chien, V. H. Schmidt, C.-S. Tu, L.-W. Hung, and H. Luo, *Phys. Rev. B* **69**, 172101 (2004).
- [12] Z. Kutnjak, J. Petzelt, and R. Blinc, *Nature (London)* **441**, 956 (2006).
- [13] Z. Kutnjak, R. Blinc, and Y. Ishibashi, *Phys. Rev. B* **76**, 104102 (2007).
- [14] M. Davis, D. Damjanovic, and N. Setter, *Phys. Rev. B* **73**, 014115 (2006).
- [15] M. Davis, *J. Electroceram.* **19**, 25 (2007).
- [16] F. Li, S. Zhang, Z. Xu, X. Wei, and T. R. Shrout, *Adv. Funct. Mater.* **21**, 2118 (2011).
- [17] H. Liu, J. Chen, L. Fan, Y. Ren, Z. Pan, K. V. Lalitha, J. Rödel, and X. Xing, *Phys. Rev. Lett.* **119**, 017601 (2017).
- [18] D. Hou, T.-M. Usher, L. Fulanovic, M. Vrabelj, M. Otonicar, H. Ursic, B. Malic, I. Levin, and J. L. Jones, *Phys. Rev. B* **97**, 214102 (2018).
- [19] R. Pirc, R. Blinc, and V. S. Vikhnin, *Phys. Rev. B* **69**, 212105 (2004).
- [20] G. Y. Xu, J. S. Wen, C. Stock, and P. M. Gehring, *Nat. Mater.* **7**, 562 (2008).
- [21] D. Fu, H. Taniguchi, M. Itoh, S.-Y. Koshihara, N. Yamamoto, and S. Mori, *Phys. Rev. Lett.* **103**, 207601 (2009).
- [22] F. Li, S. Zhang, T. Yang, Z. Xu, N. Zhang, G. Liu, J. Wang, J. Wang, Z. Cheng, Z.-G. Ye, J. Luo, T. R. Shrout, and L.-Q. Chen, *Nat. Commun.* **7**, 13807 (2016).
- [23] M. E. Manley, D. L. Abernathy, R. Sahul, D. E. Parshall, J. W. Lynn, A. D. Christianson, P. J. Stohr, E. D. Specht, and J. D. Budai, *Sci. Adv.* **2**, e1501814 (2016).
- [24] F. Li, S. Zhang, Z. Xu, and L.-Q. Chen, *Adv. Funct. Mater.* **27**, 1700310 (2017).
- [25] S. Aoyagi, A. Aoyagi, H. Osawa, K. Sugimoto, Y. Nakahira, C. Moriyoshi, Y. Kuroiwa, and M. Iwata, *Phys. Rev. B* **101**, 064104 (2020).
- [26] T. R. Welberry, D. J. Goossens, and M. J. Gutmann, *Phys. Rev. B* **74**, 224108 (2006).
- [27] M. Eremenko, V. Krayzman, A. Bosak, H. Y. Playford, K. W. Chapman, J. C. Woicik, B. Ravel, and I. Levin, *Nat. Commun.* **10**, 2728 (2019).
- [28] M. J. Cabral, S. Zhang, E. C. Dickey, and J. M. LeBeau, *Microsc. Microanal.* **22**, 1402 (2016).
- [29] M. Otoničar, A. Bradeško, L. Fulanović, T. Kos, H. Uršič, A. Benčan, M. J. Cabral, A. Henriques, J. L. Jones, L. Riemer, D. Damjanovic, G. Dražič, B. Malič, and T. Rojac, *Adv. Funct. Mater.* **30**, 2006823 (2020).
- [30] S. Dolabella, R. Frison, G. A. Chahine, C. Richter, T. U. Schulli, Z. Tasdemir, B. E. Alaca, Y. Leblebici, A. Dommanna, and A. Neels, *J. Appl. Crystallogr.* **53**, 58 (2020).
- [31] Y. Cao, T. Assefa, S. Banerjee, A. Wieteska, D. Z.-R. Wang, A. Pasupathy, X. Tong, Y. Liu, W. Lu, Y.-P. Sun, Y. He, X. Huang, H. Yan, Y. S. Chu, S. J. L. Billinge, and I. K. Robinson, *ACS Appl. Mater. Interfaces* **12**, 43173 (2020).
- [32] A. Koreeda, H. Taniguchi, S. Saikan, and M. Itoh, *Phys. Rev. Lett.* **109**, 197601 (2012).
- [33] S. Tsukada, K. Ohwada, H. Ohwa, S. Mori, S. Kojima, N. Yasuda, H. Terauchi, and Y. Akishige, *Sci. Rep.* **7**, 17508 (2017).

- [34] Y. Imai, K. Sumitani, and S. Kimura, in *Proceedings of the 14th International Conference on Synchrotron Radiation Instrumentation SRI2018*, AIP Conf. Proc. No. 2054 (AIP, Melville, NY, 2019), p. 050004.
- [35] K. Sugimoto, H. Ohsumi, S. Aoyagi, E. Nishibori, C. Moriyoshi, Y. Kuroiwa, H. Sawa, and M. Takata, in *SRI 2009, 10th International Conference on Radiation Instrumentation*, AIP Conf. Proc. No. 1234 (AIP, Melville, NY, 2010), p. 887.
- [36] G. M. Sheldrick, *Acta Crystallogr., Sect. C* **71**, 3 (2015).
- [37] Y. Kuroiwa, S. Aoyagi, A. Sawada, J. Harada, E. Nishibori, M. Takata, and M. Sakata, *Phys. Rev. Lett.* **87**, 217601 (2001).
- [38] J. Wen, G. Xu, C. Stock, and P. M. Gehring, *Appl. Phys. Lett.* **93**, 082901 (2008).